

A Novel Filter for Terrain Mapping With Laser Rangefinders

Cang Ye, Member, IEEE and Johann Borenstein, Member, IEEE

Abstract—This paper introduces a novel filter for terrain mapping with a 2-D laser rangefinder. The filter, called Certainty Assisted Spatial (CAS) filter, uses the physical constraints on motion continuity and spatial continuity to identify corrupted pixels and missing data in an elevation map. The filter removes the corrupted pixels, fills in the missing data and leaves the uncorrupted pixels intact so as to preserve the details of a terrain map. Our extensive indoor and outdoor mapping experiments show the CAS Filter’s superior performance in erroneous data reduction and map detail preservation over conventional filters.

Index Terms—laser rangefinder, terrain mapping, filtering, elevation map, certainty map, mixed pixels.

I. INTRODUCTION

Autonomous navigation of mobile robots on rugged terrain requires the capability to decide whether an obstacle should be traversed or circumnavigated. The ability to make this decision and to actually execute it is called “obstacle negotiation” (ON). A crucial issue involved in ON is terrain mapping. Research efforts on terrain mapping have been devoted to indoor environments [1], outdoor, off-road terrain [2, 3, 4], as well as planetary terrain [5, 6, 7]. Most of the existing methods employ stereovision [2, 3, 7], which is sensitive to environmental conditions (e.g., ambient illumination) and has low range resolution and accuracy. As an alternative or supplement, 3-D Laser Rangefinders (LRFs) have been employed since the early nineties [5, 6, 8]. However, 3-D LRFs are usually costly, bulky, and heavy. Therefore, they are not suitable for small and/or expendable robots. Furthermore, most of them are designed for stationary use due to the slow frame rate.

A more feasible solution for lower-cost robots is a 2-D LRF. Researchers at CMU [1] used a SICK 2-D LRF looking *upward* to perform indoor 3-D mapping. The 3-D map is not suitable for ON since no ground map is produced. Henriksen and Krotkov [9] employed an Acuity 2-D LRF to complement stereovision for obstacle and hazard detection. Due to the small look-ahead distance, the scanner was used for safety purposes only (to stop the robot in case of an emergency). More recent research at CMU [3] used a SICK LMS 220 (with a range up to 32 m and a field of view of 100°) on the “Nomad” robot. The LRF “looks” diagonally downward and forward. As the robot moves forward, the fanning laser beam swept the ground ahead of the robot and produced terrain data. Based on the data, a so called “goodness map,” was created by comparing the current scan data with the previous ground level (a least square fit line in the previous scan). The “goodness map” was then combined with the map built by stereovision for path planning. In this work, the overall map was produced mainly by stereovision.

This paper presents a new terrain mapping method using a single sensor modality—a 2-D LRF, and an innovative filtering method for map building. The paper is organized as follows: In Section II, we introduce our approach to terrain mapping. In Section III, we present experimental results and discuss the computational cost of the filter. In Section IV, we compare our filter to other related mixed pixel removal methods and discuss the real-time implementation issues.

II. MAP BUILDING AND FILTERING ALGORITHM

A. Map building principle

As depicted in Fig. 1, a SICK LMS 200 is mounted on our “Gorilla” vehicle such that the LRF looks diagonally forward and downward at a pitch angle of -11° . While the vehicle is in motion, the fanning laser beam sweeps the terrain ahead of the vehicle and produces continuous range measurements of the terrain. For the experiments described in this paper, we set our LRF to an angular resolution of 1° and a serial communication speed of 500 Kbaud. Under these conditions, the LRF produces 181 range readings for its 180-degree field of view every 13.3 ms (see [10] for details).

Our algorithm assumes that real-time, 6-degree-of-freedom pose information is available from our so-called Proprioceptive Pose Estimation (PPE) system, which is described in detail in [11]. With the pose information avail-

able, the range data can be transformed into world coordinates and registered into a terrain map. The terrain map consists of an elevation map and a certainty map. Both are 2-D grid-type maps. Each cell in the elevation map holds a value that represents the height of the object at that cell, while each cell in the certainty map holds a value that expresses our certainty in the accuracy of the corresponding cell in the elevation map.

In order to project raw range data onto the 2-D elevation map, we use the Euler transformation. The forward kinematic transformation is given by:

$$\bar{d}^n = T_l^n \bar{d}^l \quad (1)$$

where $\bar{d}^n = (x_n, y_n, z_n)^T$ and $\bar{d}^l = (x_l, y_l, z_l)^T$ are the range measurements in the world coordinate system and in the LRF coordinate system, respectively. T_l^n is the forward kinematic transformation matrix. For conciseness, we omit the derivation of the transformation matrix here.

To study the mapping characteristics under well-controlled conditions, we use the experimental setup shown in the left of Fig. 2. The LRF is mounted on a rotary table, which produces roll and pitch rotation. The linear motion table

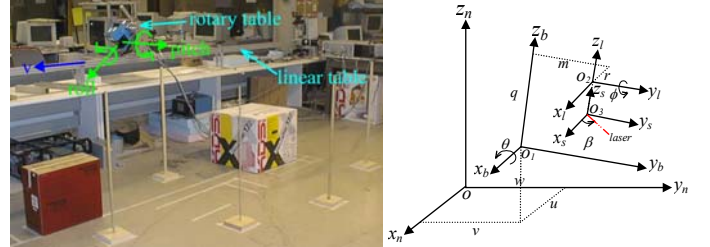


Fig. 2. Experimental setup and the coordinate systems for terrain mapping study: the linear motion table moves the LRF at velocity v (max.: 1 m/s) and the rotary table tilts the LRF at a maximum rate of 37.5°/s in a range of $[-15^\circ, 15^\circ]$ for roll and $[-40^\circ, -25^\circ]$ for pitch.

produces linear motion for the rotary table. This experimental setup emulates to some extent the motion of a mobile robot on rugged terrain.

The coordinate systems for the experimental setup are depicted in the right of Fig. 2. They consist of the world coordinate system $x_n y_n z_n$, the coordinate systems attached to the rotary table $x_b y_b z_b$ and $x_l y_l z_l$, and the LRF coordinate system $x_s y_s z_s$. The coordinate values of o_3 in $x_l y_l z_l$, o_2 in $x_b y_b z_b$, and o_1 in $x_n y_n z_n$ are (θ, ϕ, p) , (t, m, q) , and (u, v, w) , respectively.

The forward kinematic transformation is given by

$$\begin{pmatrix} x_n \\ y_n \\ z_n \end{pmatrix} = \begin{pmatrix} lc\phi c\beta + ps\phi + r + u \\ lc\theta s\beta + ls\theta s\phi c\beta - qs\theta + mc\theta - ps\theta c\phi + v \\ ls\theta s\beta - lc\theta s\phi c\beta + qc\theta + ms\theta + pc\theta c\phi + w \end{pmatrix} \quad (2)$$

where sx stands for $\sin(x)$ and cx stands for $\cos(x)$. β is the angle between the k^{th} laser beam (which produces range measurement l) and the x_s -axis and is given by

$$\beta = (k-1)\pi/180 \quad (3)$$

For every two consecutive measurements at time steps t and $t+1$, the maximum change of height value Δz for the measurement at (x_n, y_n) is calculated by

$$\Delta z_{\max}^t = -\Delta y \tan \theta + \frac{\partial z_n}{\partial l} \Delta l + \frac{\partial z_n}{\partial \theta} \Delta \theta + \frac{\partial z_n}{\partial \phi} \Delta \phi \quad (4)$$

where Δy is the displacement of the LRF along the y_n axis, δl is the maximum measurement error of the LRF (32 mm according to [10]), $\partial z_n / \partial l$, $\partial z_n / \partial \theta$, and $\partial z_n / \partial \phi$ are partial derivatives that can be derived from Eq. 2.

In this paper, a grid cell size of 25×25 mm is used such that each cell may be illuminated one time even if the vehicle moves at the maximum speed of 1 m/s. A cell in the elevation map is denoted $h(i, j)$, while a cell in the certainty map is denoted $c(i, j)$. Using the above transformation the coordinate values x_n and y_n are computed for each range measurement at time t and mapped to the grid indices i and j , respectively. Then, pixel $c(i, j)$ in the certainty map is updated as follows:

$$c^{t+1}(i, j) = \begin{cases} c^t(i, j) + a & \text{if } |z_n^{t+1} - h^t(i, j)| \leq |\Delta z_{\max}^t| \text{ or } c^t(i, j) = 0 \\ c^t(i, j) & \text{otherwise} \end{cases} \quad (5)$$

where $a \geq 1$ is the increment of the certainty value and it can be any positive integer (we use 3 in this study). The pixel $h(i, j)$ in the elevation map is updated by

$$h^{t+1}(i, j) = \begin{cases} z_n^{t+1} & \text{if } |z_n^{t+1}| > |h^t(i, j)| \\ h^t(i, j) & \text{otherwise} \end{cases} \quad (6)$$

In every 13.3-millisecond interval the 181 range measurements acquired from the LRF are mapped into both maps.

B. Sources of mapping errors

Ideally, a terrain map built according to the above-described algorithm should be sufficient for navigating a mobile robot. However, some range data from the SICK LMS 200 are erroneous and will cause mapping errors. The phenomenon of mixed pixels, missing data, and artifacts/noise are the main sources of erroneous measurements: (1) Mixed pixels occur when a laser beam hits the very edge of an object so that part of the beam is reflected from that edge of the object and part of the beam is reflected from the background behind the object. The resulting range measurement lies somewhere between the distance to the object and the distance to the background [10]. In researching the mixed pixels phenomenon, we found that if the distance ΔD between the edge of the foreground object and the background is close to the length of the laser pulse, ΔL ($\Delta L \approx 1$ m for the SICK LRF¹), a substantial number of mixed pixels are generated. However, if $\Delta D > \Delta L$, the number of mixed pixels drops significantly (see Fig. 3). This is because the SICK LRF is designed to accept only reflections stemming from the same pulse¹ as valid data. This smart design is effective in rejecting ambient noise. Fig. 3 shows that mixed pixels exist even if ΔD is as big as 1.6 meter. Another characteristic of mixed pixels is that a small change in an edge's lateral position with reference to the laser beam may induce a large change in the measured range. (2) Missing data occur when the measured range is invalid [12]. For instance, no return or too weak a returned signal may result in missing data; direct exposure to the sunlight may lead to dazzling and cause invalid readings. For a complete list of the SICK LRF's error conditions see [12]. (3) Environmental interferences, such as ambient light and shock during motion, may potentially create noisy range measurements and hence result in noise in the elevation map. The analysis of LRF noise is treated in [13].

Fig. 4 shows the effects of these errors. Such errors in the terrain map deteriorate the ON performance of the vehicle.

C. Conventional image filtering algorithms

An elevation map can be transformed into a range image, in which the height value of each pixel is represented by intensity. This way conventional image processing filters [14, 15, 16] can be applied to the elevation map in an attempt to eliminate the above-discussed erroneous data.

However, the application of conventional image filtering techniques is not without drawbacks. The foremost reason is that most conventional image filtering methods are unconditionally applied to the entire range image and may thus blur the image. Convolution-based frequency filters, such as the Averaging Filter, Gaussian Filter [15], or Wiener Filter [16], are implemented

by the convolution of an input image with a convolution kernel in the spatial domain.

The effect is that noise is suppressed but the objects in the image are

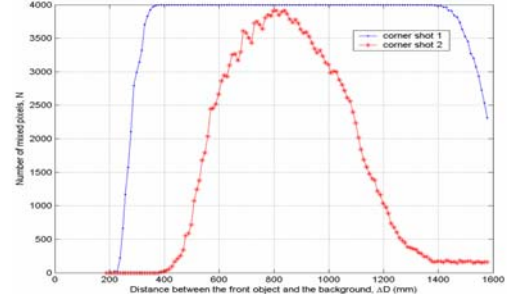
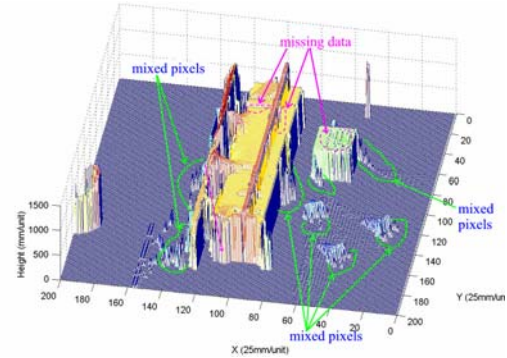
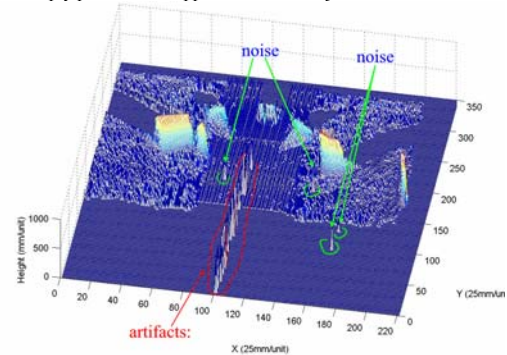


Fig. 3. Characteristics of mixed pixels: 4000 range measurements were taken at each point. A measurement is determined as a mixed pixel if the difference between the measured range and the foreground/background is bigger than 60 mm. Large numbers of mixed pixels are generated when the distance ΔD between the edge of the foreground object and the background is close to the length of a pulse of the laser, ΔL . However, if $\Delta D > \Delta L$, then the number of mixed pixels drops significantly.



(a) Mixed pixels can create phantom objects behind the edges of objects. Missing data creates empty pixels in the upper surfaces of objects.



(b) Environmental interferences can cause artifacts/noise. In the 16-meter measuring mode of the SICK LRF, we observed that there are a lot of high spikes (labeled “artifacts”) in the center of this terrain map, which was built on a flat sidewalk near our lab. Close examination revealed that most of these artifacts resulted from very small range measurements, which may be removed by threshold. We suspect that undetected overflow is the cause. The other high spikes are the result of random noise in range data, which produces range errors at several meters ahead of the LRF.

Fig. 4. Map misrepresentation due to range errors

blurred at the same time. Filters based on Anisotropic Diffusion [17] diffuse more in smooth areas and less around large intensity transitions, thus small variations in image intensity (i.e., those that are caused by noise) are smoothed and edges are preserved. However, mixed pixels may create large phantom objects, which look like edges rather than like noise, along the edges of objects. It may be difficult to smooth them based on the gradient of intensity without diffusing the edges.

Median Filters have the advantage of not introducing any new pixel into the images, thereby preserving details. Median Filters have been used to remove mixed pixels in laser range images [14]. The standard Median Filter and its variations (Weighted Median Filter [18] and Center Weighted Median Filter [19]) often exhibit blurring when a large filter window is used, or

¹ Base on our communication with SICK in Germany, the LRF is a single shot measurement system. It sends out a pulse with a width close to 1 m and expects a reflected signal with the same pulse width; received signals of other pulse widths are rejected. At a corner shot, the LRF may receive reflection from both the edge and the background if the distance between them is within the pulse width. This results in mixed pixels.

insufficient noise reduction for a small filter window. Adaptive Median Filters [20, 21] maintain a better balance between detail preservation and noise reduction, and hence achieve better performance. However, all of these median-type filters affect all the pixels in an image including uncorrupted ones. A number of median type filters in the scientific literature [22, 23] may potentially distinguish corrupted pixels from uncorrupted ones and apply filtering only to the corrupted pixels. These filters utilize local input image characteristics to identify corrupted pixels. However, a limitation of this approach is the potential misclassification of thin edges as corrupted pixels and the subsequent removal of these pixels. For instance, a thin pole in a range image produces a line of high intensity pixels, which may be misinterpreted by the filter as impulse noise and may therefore be removed. Based on this discussion, we summarily conclude that it is insufficient to use only spatial information for reliable identification and removal of corrupted pixels.

D. The Certainty Assisted Spatial (CAS) Filter

In this paper, we propose a novel filter for elevation map building. The filter is called ‘‘Certainty Assisted Spatial’’ (CAS) filter. This filter utilizes not only the spatial information contained in the unfiltered elevation map, but also the certainty information contained in the certainty map, as explained in Section II. A.

Due to the continuity of motion, every two consecutive measurements on the edge of a real object satisfy $|z_n^{t+1} - h^t(i, j)| \leq |\Delta z_{\max}^t|$. According to Eq. 5, edge pixels are assigned continuous certainty increments and result in large certainty values in the certainty map. Therefore, edge pixels in the elevation map can be identified easily. They are preserved and no filtering is applied. Mixed pixels may occur somewhere between the edges of objects and the background. Their locations are determined by the percentage of laser spots hitting the background [10]. When the LRF is in motion, as it necessarily is for mapping, this percentage changes all the time. Consequently, mixed pixels keep changing their x - and y -coordinates all the time. This means that the condition $|z_n^{t+1} - h^t(i, j)| \leq |\Delta z_{\max}^t|$ is not satisfied. Hence, mixed pixels usually have small certainty value and are spatially isolated in both the elevation map and the certainty map. They can be identified and removed easily. Artifacts and random noise have the same characteristics and can also be removed by the same principle. Finally, missing data create empty pixels in an elevation map and their certainty values are zero. We found that applying a Weighted Median Filter to those pixels with zero certainty values can supply (interpolate) the missing data. The filtering process works as follows:

Let $H = \{h(i, j) \mid 1 \leq i \leq M, 1 \leq j \leq N\}$ and $C = \{c(i, j) \mid 1 \leq i \leq M, 1 \leq j \leq N\}$ denote the elevation map and the certainty map, respectively, where M is the length and N is the width of the map. A filter with a window size of $(2k+1) \times (2k+1)$ (in this paper we use $k=2$) is defined symmetrically surrounding the current pixel $h(i, j) \in H$. The current pixel $h(i, j)$ is updated by the output of the filter, which is given by

$$y(i, j) = \begin{cases} 0 & \text{if } c(i, j) \leq A \text{ and } g_s(i, j) = 0 \text{ and } g_c(i, j) = 0 \\ y_{wm}(i, j) & \text{else if } g_s(i, j) = 1 \text{ and } c(i, j) = 0 \\ h(i, j) & \text{otherwise} \end{cases} \quad (7)$$

and

$$A = a \times (\text{int}(s/v\Delta t) + 2) \quad (8)$$

where $\text{int}(\bullet)$ means round to the nearest integer, s is the grid cell size, v is the linear velocity of the LRF (the maximum is 1 m/s in this paper) and $\Delta t = 13.3$ ms is a time step. In this equation, $\text{int}(s/v\Delta t)$ is the estimate on the number of times a grid is illuminated. In order to filter the mixed pixels at the vicinity of the edges, a constant value of 2 is added. $g_s(i, j)$ and $g_c(i, j)$ are the spatial continuity index of H and C for the pixels in the filter window, respectively. They are expressed by

$$g_s(i, j) = \begin{cases} 0 & \text{if } \sigma_{\bar{h}}(i, j) > B \\ 1 & \text{otherwise} \end{cases} \quad (9)$$

and

$$g_c(i, j) = \begin{cases} 0 & \text{if } \sum_{m=i-k, n=j-k}^{i+k, j+k} c(m, n) < G \text{ or } \sigma_{\bar{c}}(i, j) > E \\ 1 & \text{otherwise} \end{cases} \quad (10)$$

where $\sigma_{\bar{h}}$ and $\sigma_{\bar{c}}$ are the variance of the normalized local maps \bar{H}_L and \bar{C}_L normalized by the maximum elevation and certainty values, respectively.

We use $10 \times A$ for G and 0.04 for E . To keep the computational cost low we

use $\sum_{m=i-k, n=j-k}^{i+k, j+k} \bar{H}_L < 7$ to approximate the condi-

tion $\sigma_{\bar{h}}(i, j) > B$ in Eq. 9. $y_{wm}(i, j)$ is the output of a Weighted Median (WM) filter centered at pixels (i, j) . The input pixels to the WM filter are obtained by applying a filter skeleton [18] (as depicted in Fig. 5) to the elevation map. For instance, $h(i, j)$ has one

	$j-2$	$j-1$	j	$j+1$	$j+2$	
	2	2	2	2	2	$i-2$
	2	2	1	2	2	$i-1$
	2	1	1	1	2	i
	2	2	1	2	2	$i+1$
	2	2	2	2	2	$i+2$

Fig. 5. Filter skeleton for the proposed WM filter

copy, while $h(i-2, j-1)$ has two copies in the input pixels to the WM filter. The use of this skeleton is based on the following heuristic: Since we suspect $h(i, j)$ to be a missing datum, the nearest neighboring pixels $h(i \pm 1, j \pm 1)$ are also likely to be missing data, while those pixels farther from $h(i, j)$ have a greater likelihood not to be missing data. Note, however, that this weight assignment for the WM filter potentially removes more missing data on the upper surface of an object.

When the CAS Filter is applied to the raw elevation map, mixed pixels, artifacts, and random noise are identified by examining the motion continuity (i.e., $c(i, j)$ constrained by Eq. 5) and the spatial continuity in the elevation map and the certainty map ($g_s(i, j)$ and $g_c(i, j)$). Missing data is distinguished by inspecting the current pixel’s certainty value $c(i, j)$ and the spatial continuity $g_s(i, j)$ in the elevation map. Mixed pixels, artifacts, and random noise are therefore removed and the missing data are filled by the WM filter.

III. EXPERIMENTAL RESULTS

In this section, we present extensive experimental results. These results can be grouped into two categories: Benchmark tests performed under highly controlled conditions, and mobility tests in which the LRF was mounted on a mobile platform. In all of the experiments, we used a 1.2 GHz AMD Athlon processor-based PC running RT-Linux for the real-time data collection.

A. Benchmark Tests

Based on the experimental setup in Fig. 2, we designed the following four benchmark tests: 1) The LRF translates only (denoted ‘T’); 2) the LRF translates and rotates with roll only (denoted ‘TR’); 3) the LRF translates and rotates with pitch only (denoted ‘TP’); and 4) the LRF translates and rotates with roll and pitch (denoted ‘TRP’).

For the experiments described here, we built 16 obstacle courses as listed in Table I (e.g., obstacle course #6 comprises parallelepiped 1&2, the cylinder, pole 1-4 and pole 6). The performance of our CAS Filter is compared with that of the Wiener Filter, the Averaging Filter, the Median Filter, and the Center Weighted Median (CWM) Filter. Fig. 6 shows the 4th obstacle course, while Fig. 7 depicts the raw and filtered elevation maps based on benchmark test T with different filters. It can be observed that the CAS Filter preserves more original pixels, removes most of the mixed pixels, and fill almost all of the missing data. The Wiener Filter retains almost all missing data, and some mixed pixels, but it only smooths some other mixed pixels. The Median Filter and the CWM Filter over-filter the poles while the Averaging Filter distort the map significantly. Examination on all other tests reveals that the CAS filter preserved all poles (as small as 2.5 mm in diameter) while successfully removing the mixed pixels.



Fig. 6. One of the 16 indoor obstacle courses.

Table I: Features of the 16 obstacle courses

Obstacle layout	Parallelepiped				Cylinder	Poles
	1	2	3	4		
1		X	X			1-5, 7, 9
2			X			1-7, 9
3						1-7, 9
4		X		X	X	1, 2, 4, 6
5	X	X				1-4, 6
6	X	X			X	1-4, 6
7	X	X			X	1-7
8		X		X	X	1-9
9		X		X		1-9
10		X	X	X		1-5, 7, 9
11	X	X	X			1-5, 7, 9
12		X		X		1-5, 7, 9
13		X	X			1-7, 9
14	X	X	X			
15		X	X	X		
16		X	X			

Dimensions of parallelepiped objects (all units in mm):

#1: 530×559×462, #2: 413×456×414, #3: 400×343×213, #4: 514×540×327

Dimensions of poles: #1-#9 have diameters of 24, 21, 19, 15, 11, 9, 6, 4.5 and 2.5, respectively and a length of 914.

Dimension of cylinder: diameter=411, height= 459

For each of the 16 obstacle courses, we performed four different tests, namely, the T, TR, TP, and the TRP test, as described in the beginning of this section. The results are summarized in Fig. 8. It is evident from these results that our proposed CAS Filter consistently outperformed the four conventional filters. The relatively poor performance of the Median Filter and the CWM Filter is due to their inherent over-filtering. On the other hand, when roll and pitch motion was added to the translatory motion, the CAS Filter performed only marginally better than the Wiener Filter (and the Averaging Filter in some instances). This is due to the following observations: (1) Roll and/or pitch motion potentially increased mapping errors because they caused vibrations of the rotary table and changes in occlusions. According to Eq. 11, these additional errors move the CAS Filter's PI close to that of the Wiener and Averaging filter. (2) Roll and pitch motion may increase the amount of empty pixels on the objects' upper surfaces. When the number of empty pixels in the

filter window is above a certain value, the CAS Filter removes the current pixel, while the Wiener Filter or the Averaging Filter replace the current pixel with a spatial convolution value. However, the deterioration of the CAS Filter's PI does not mean that the Wiener Filter and Averaging Filter are more suitable for ON. This is because the Wiener Filter does not remove artifacts/noise in elevation maps (see Section III. B), while the Averaging Filter tends to lower the height of edges in the elevation maps—a highly undesirable trait.

In order to compare the filter performance in a quantitative way, we measured by hand the exact location of each obstacle in each obstacle course and converted these measurements into a ground truth elevation map. We then evaluate the performance of filter by computing an overall index of performance (PI) according to

$$PI = \frac{\sum_{j=1}^N \sum_{i=1}^M (h_f(i, j) - h_t(i, j))^2}{\sum_{j=1}^N \sum_{i=1}^M (h_r(i, j) - h_t(i, j))^2} \quad (11)$$

where $h_r(i, j)$, $h_t(i, j)$ and $h_f(i, j)$ are the elevation values of pixel (i, j) in the raw elevation map, the ground truth map, and the filtered map, respectively. We arbitrarily selected $M=80$ and $N=200$ (which has full coverage of all obstacle courses) to evaluate the experiments here. According to Eq. 11, a smaller PI means better filter performance.

Note: We found that the inclusion of $\sigma_{\epsilon}(i, j) > 0.04$ in the benchmark tests did not improve the filter's performance significantly. Therefore, we dropped this term to save computation in ON applications.

B. Experimental results on a mobile robot

We carried out a number of indoor and outdoor map building experiments with the LRF on our Gorilla vehicle (see Fig. 1). However, these experiments were limited to straight-line motion on flat, horizontal ground. More diverse terrain would require real-time pose data from our PPE system, which we have not yet integrated with the ON application described here. Fig. 9 shows the obstacle courses and the vehicle in our indoor and outdoor mapping experiments.

From the maps depicted in Fig. 10, it is apparent that the CAS Filter outperforms the Wiener Filter because it almost completely removes mixed pixels

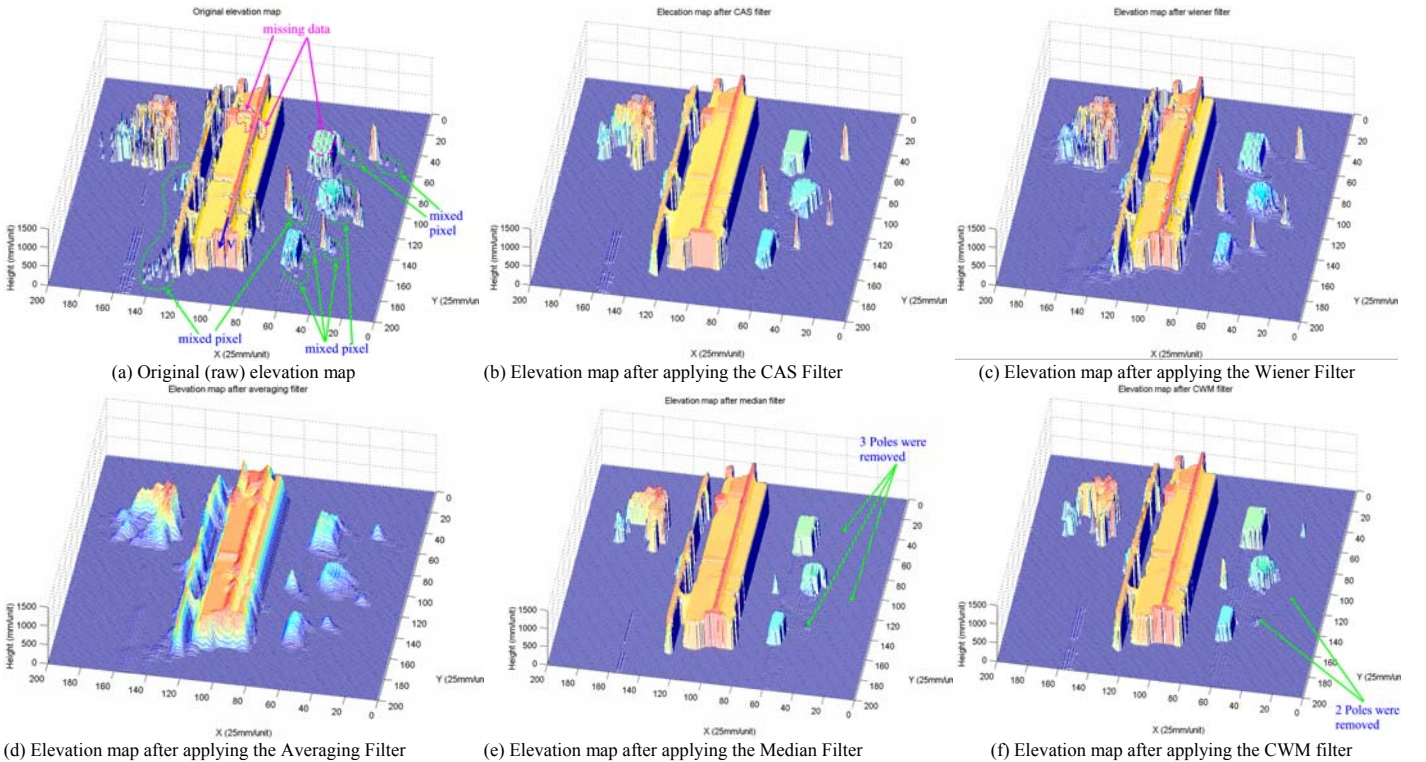


Fig. 7. Original elevation map and the maps after applying the five tested filters: the linear motion table moved the LRF along the direction 'v'

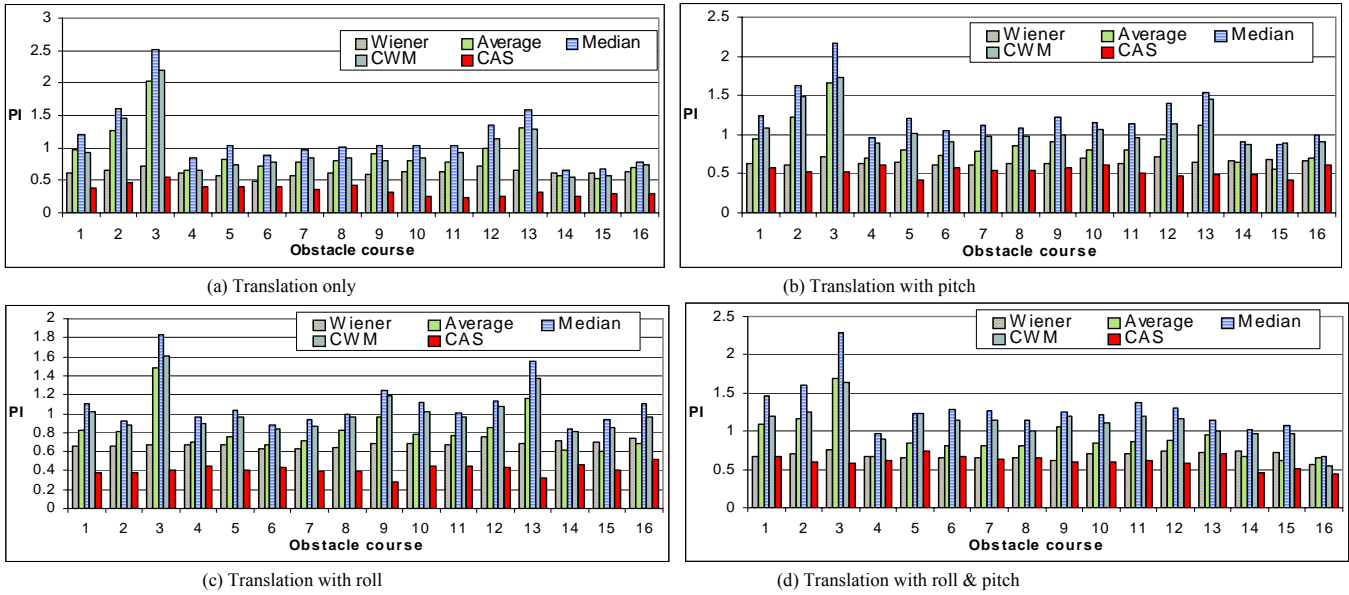


Fig. 8. Comparison of filter performance



Fig. 9. Obstacle courses for mapping: left: indoor, right: outdoor

and fills most of the missing data on the top surfaces of objects (see Fig. 10(b)).

In contrast, the Wiener Filter leaves some noticeable mixed pixels and most of the missing data in the map, as shown in Fig. 10(c). In the outdoor mapping experiment (see Fig. 11), the CAS Filter completely removed all artifacts and random noise, while the Wiener Filter did not remove any.

C. Preservation of details and computational cost

The preservation of details and computational cost of the CAS Filter depends on each case and we are unable to provide a general analytical analysis. However, we can give a preliminary estimate based on the benchmark tests. Table II shows the percentage of pixels identified by the CAS Filter as mixed pixels and missing data in benchmark test ‘T’. For the worst case (the 3rd obstacle course) in the 16 obstacle courses, 74.8% of pixels were left intact. This means that the CAS Filter preserved a significant amount of details,

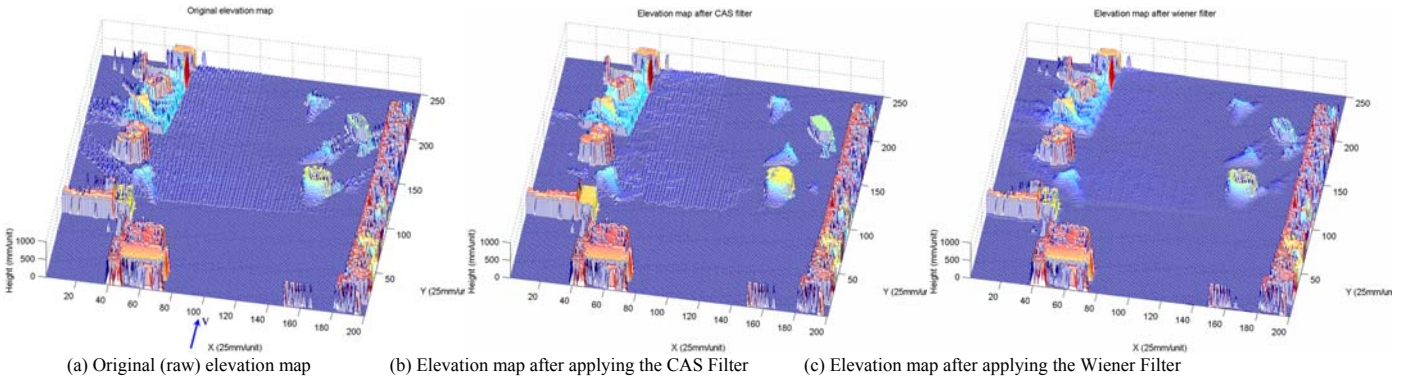


Fig. 10. Indoor elevation maps: the vehicle moved along direction v

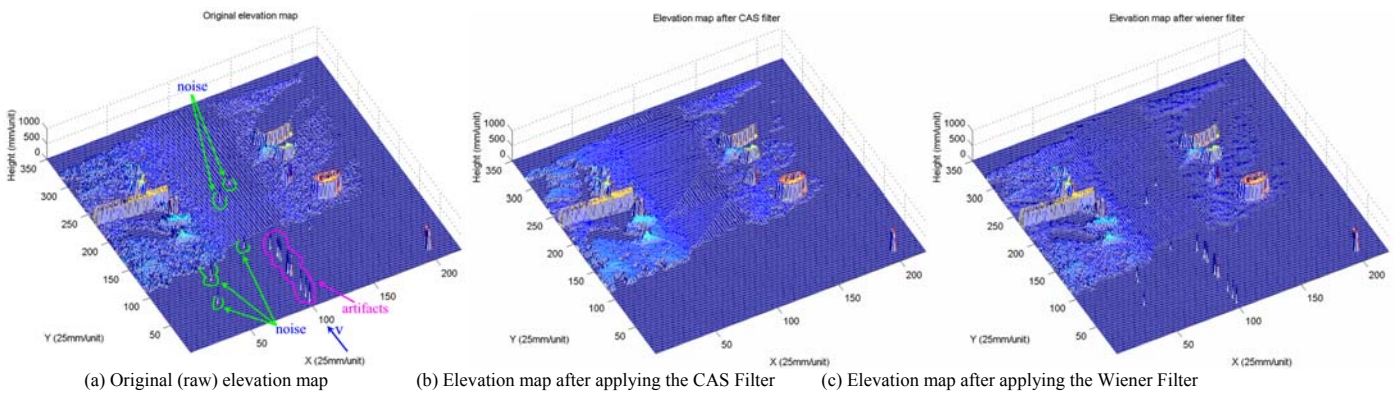


Fig. 11. Outdoor elevation maps: the vehicle moved along direction v

TABLE II. PERCENTAGE OF PIXELS IDENTIFIED AS CORRUPTED IN BENCHMARK TEST ‘T’

Obstacle courses	1	2	3	4	5	6	7	8	9	10	11	12	13	14	15	16
Mixed pixels	17.8	16.7	17.6	15.0	15.9	16.7	16.2	17.5	17.5	16.8	16.0	13.4	16.1	12.1	11.4	13.4
Missing data	5.6	6.0	7.6	6.4	6.4	6.5	6.2	6.4	6.5	6.2	6.5	4.9	4.4	4.5	4.5	4.2
No filtering	76.6	77.3	74.8	78.6	77.7	76.8	77.6	76.1	76	77	77.5	81.7	79.5	83.4	84.1	82.4

Note: The total number of pixels in the maps is 200×200, of which only 196×196 pixels are processed by the CAS Filter.

which is also the main motive for the development of the CAS Filter.

For an estimate on computational cost, we compared the CAS Filter with the standard Median Filter. From Equations (7)-(10), we can determine that in order to process the pixels in a row ($K=196$), the CAS Filter requires: $2P+11K-12$ additions, $2K-2$ subtractions, $3K$ multiplications and K divisions. The algorithm further incurs complexity $0.076 \times KQ \lg Q$ in the WM filter and $K(P-1)$ in comparison (to find the maximum). $P=25$ and $Q=45$ are the number of pixels in the filter windows and the number of pixels in the WM filter skeleton (Fig. 5), respectively. The Median Filter has a complexity of $KP \lg P$. For integer operation in the PC used in the experiment, we found: (1) the four fundamental operations of arithmetic and the sorting operation have roughly the same computational cost, 1.7 ns; and (2) a comparison operation has a cost of 0.085 ns. Considering the worse case (the 3rd obstacle course), the estimated average computing time of the CAS Filter is 12.2 ms, while that of the Median Filter is 38.7 ms. This means that the CAS Filter is less expensive in computation than the Median Filter. Although it requires additional computation in building the certainty map (Eq. 4 & 5), this is not significant. Thus we believe that the CAS Filter is computationally more efficient than the Median Filter. An examination of the other benchmark tests revealed similar results, which we omit here because of space limitations.

IV. DISCUSSION

A. Comparison to other mixed pixels removal methods

We are aware that there is an alternative to filtering mixed pixels. Adams [24] proposed an efficient mixed pixels removal method for phase-shift LRFs. The algorithm is based on the detection of discontinuity of the received signal’s amplitude. However, due to the difference of measuring principles (time-of-flight in the case of the SICK LRF), this method must be modified to suit the SICK LRF. Such modification requires knowledge of the internal physics and the hardware design of the LRF, and can thus be implemented effectively only by the manufacturer, not the user. Specifically, Adam’s discontinuity detection algorithm requires several samples of the received signal (for computing the second derivative of the square of the signal amplitude with respect to the area illuminated by the laser on the edge) during the time the laser beam traverses the edge. However, at user level, we can only get a single measurement on the edge. This means that it is impractical to implement this algorithm.

Finally, our method is based on the characteristics of the erroneous data and the motion continuity constraint and it is thus device independent. Therefore, it is more general and suitable for the end users of LRFs. In contrast to Adams’ algorithm, our approach removes not only mixed pixels but also unexpected outdoor artifacts and noise.

B. Real-time implementation issues

The CAS Filter can be used for mapping where off-line processing is sufficient. For real-time obstacle negotiation, the CAS Filter can be implemented as follows: within the computer’s world model, a so-called *active window* of size 200×400 pixels (rows × columns) travels with the vehicle. The LRF is located at the center of the first row. In each LRF sampling period, only the pixels (in both elevation & certainty map) from the $(200-m)^{\text{th}}$ row to the 200^{th} row ahead of the vehicle are updated. Then the pixels in row $200-m$ is filtered and registered into another elevation map, which is used for obstacle negotiation. m is chosen in such a way that the vehicle can acquire sufficient obstacle/terrain information in elevation. The grid cell size of the elevation map for obstacle negotiation may be bigger than 25×25 mm subject to application.

Our terrain mapping method requires real-time vehicle pose information, which will be obtained by our PPE system. Therefore, it is not necessary to perform simultaneous localization and mapping in our method. The PPE system was proposed in [11] and the researchers at our lab have already built this system. We will integrate this system into our mapping method in the immedi-

ate future.

V. CONCLUSIONS

In this paper, we presented a novel filter for terrain mapping with a 2-D LRF. The terrain map consists of an elevation map and a certainty map. The value of each pixel in the certainty map is determined as a function of a so-called “motion continuity constraint.” Typical erroneous data, such as mixed pixels, artifacts, and random noise don’t satisfy the motion continuity constraint and thus result in a low certainty value. Examination of the appropriate pixels in both maps allows our CAS Filter to identify mixed and missing pixels. This distinction, in turn, allows the CAS Filter to apply different treatments to these different conditions. Uncorrupted pixels are left intact to preserve the map details.

Overall, our proposed CAS Filter produces consistently better results than conventional filtering algorithms because it makes use of the additional information available in the certainty map.

ACKNOWLEDGMENT

This work was funded by the U.S. Department of Energy under Award No. DE-FG04-86NE3796 and under a grant from The University of Michigan’s Automotive Research Center (ARC), funded by TACOM. The authors would like to thank Mr. Weber, SICK Germany for his kind help and insightful advice on the LRF. The authors would also like to thank James Berry for his work on the design of the rotary table.

REFERENCES

- 1 S. Thrun, W. Burgard and D. Fox, “A real-time algorithm for mobile robot mapping with application to multi-robot and 3D mapping,” *Proc. IEEE Int. Conf. Robotics and Automation*, 2000, pp. 321-328.
- 2 S. Betgé-Brezetz, et al, “Uncertain map making in natural environments,” *Proc. IEEE Int. Conf. Robotics and Automation*, 1996, pp. 1048-1053.
- 3 D. S. Apostolopoulos, et al, “Technology and field demonstration of robotic search for Antarctic meteorites,” *Int. J. Robotics Research*, vol. 19, no. 11, pp. 1015-1032, 2000.
- 4 K. Fregene, R. Madhavan and L. E. Parker, “Incremental multi-agent robotic mapping of outdoor terrain”, *Proc. IEEE Int. Conf. Robotics and Automation*, 2002, pp. 1339-1346.
- 5 I. S. Kweon and Takeo Kanade, “High-resolution terrain map from multiple sensor data,” *IEEE Trans. Pattern Anal. Machine Intell.*, vol. 14, no. 2, pp. 278-292, 1992.
- 6 E. Krotkov and R. Hoffman, “Terrain mapping for a walking planetary rover,” *IEEE Trans. Robot. Automat.*, vol. 10, no. 6, pp. 728-738, 1994.
- 7 R. Simmons, et al, “Experience with rover navigation for lunar-like terrains,” *Proc. IEEE/RSJ Int. Conf. Intelligent Robots and System*, 1995, pp. 441-446.
- 8 C. M. Shoemaker and J. A. Bornstein, “The demo III UGV program: a testbed for autonomous navigation research,” *Proc. IEEE ISIS/CIRA/ISAS Joint Conference*, 1998, pp. 644-651.
- 9 L. Henriksen and E. Krotkov, “Natural Terrain Hazard Detection with a Laser Range-finder,” *Proc. IEEE Int. Conf. Robotics and Automation*, 1997, pp. 968-973.
- 10 C. Ye and J. Borenstein, “Characterization of a 2-D laser scanner for mobile robot obstacle negotiation,” *Proc. IEEE Int. Conf. Robotics and Automation*, 2002, pp. 2512-2518.
- 11 L. Ojeda and J. Borenstein, “FLEXnav: Fuzzy Logic Expert Rule-based Position Estimation for Mobile Robots on Rugged Terrain,” *Proc. IEEE Int. Conf. Robotics and Automation*, 2002, pp. 317-322.
- 12 SICK Inc., *LMS/LMI Telegram Listing*, version 05.00, page 98.
- 13 D. Nitzan, et al, “The measurement and use of registered reflectance and range data in scene analysis”, *Proceedings of the IEEE*, vol. 65, no. 2, 1977.
- 14 M. Hebert and E. Krotkov, “3D measurements from imaging laser radars: how good are they?” *Image and Vision Computing*, vol. 10, no. 3, pp. 170-178, 1992.
- 15 C. F. Olson, “Adaptive-scale filtering and feature detection using range data”, *IEEE Trans. Pattern Anal. Machine Intell.*, vol. 22, no. 9, 2000.
- 16 A. K. Jain, *Fundamentals of Digital Image Processing*, Prentice Hall, 1989.
- 17 P. Perona and J. Malik, “Scale-space and edge detection using anisotropic diffusion”, *IEEE Trans. Pattern Anal. Machine Intell.*, vol. 12, no. 7, 1990.
- 18 D. R. K. Brownrigg, “The weighted Median Filter,” *Communication of the ACM*, vol. 27, no. 8, pp. 807-818, 1984.

- 19 S. Ko and S. Lee, "Center weighted Median Filters and their applications to image enhancement," *IEEE Trans. Circuits and Systems*, vol. 38, no. 9, pp. 984-993, 1991.
- 20 H. Lin and A. N. Willson, Jr., "Median Filters with adaptive length," *IEEE Trans. Circuits and Systems*, vol. 35, no. 6, 1988.
- 21 T. Chen and H. R. Wu, "Application of partition-based median type filters for suppressing noise in images," *IEEE Trans. Image Processing*, vol. 10, no. 6, pp. 829-836, 2001.
- 22 H. Eng and K. Ma, "Noise adaptive soft-switching Median Filter," *IEEE Trans. Image Processing*, vol. 10, no. 2, pp. 242-251, 2001.
- 23 T. Chen, K. Ma and L. Chen, "Tri-state Median Filter for image denoising," *IEEE Trans. Image Processing*, vol. 8, no. 12, pp. 1834-1838, 1999.
- 24 M. D. Adams and P. J. Probert, "The interpretation of phase and intensity data from AMCW light detection sensors for reliable ranging", *Int. J. Robot. Res.*, vol. 15, No. 5, pp. 441-458, 1996.